FLOW CAMBRIDGE UNIVERSITY PRESS

RESEARCH ARTICLE

Hopper flows of dense suspensions: a 2D microfluidic model system

Lars Kool[1,2,*] , Jules Tampier[1,*] , Philippe Bourrianne[1] and Anke Lindner[1,3]

[1]Laboratoire de Physique et Mécanique des Milieux Hétérogènes (PMMH), CNRS, ESPCI Paris, Université PSL, Sorbonne Université, Université Paris Cité, Paris, France
[2]Plateforme Technologique, CNRS UAR3750, Institut Pierre-Gilles de Gennes (IPGG), ESPCI Paris - PSL, Paris, France
[3]Institut Universitaire de France (IUF), Paris, France
Corresponding author: Anke Lindner; Email: anke.lindner@espci.fr

Abstract

Flows of particles through bottlenecks are ubiquitous in nature and industry, involving both dry granular materials and suspensions. However, difficulties in precisely controlling particle properties in conventional set-ups hinder the full understanding of these flows in confined geometries. Here, we present a microfluidic model set-up to investigate the flow of dense suspensions in a two-dimensional hopper channel. Particles with controlled properties such as shape and deformability are *in situ* fabricated with a photolithographic projection method and compacted at the channel constriction using a Quake valve. The set-up is characterised by examining the flow of a dense suspension of hard, monodisperse disks through constrictions of varying widths. We demonstrate that the microfluidic hopper discharges particles at a constant rate under both imposed pressure and flow rate. The discharge of particles under imposed flow rate follows a Beverloo-like scaling, while it varies nonlinearly with particle size under imposed pressure. Additionally, we show that the statistics of clog formation in our microfluidic hopper follow the same stochastic laws as reported in other systems. Finally, we show how the versatility of our microfluidic model system can be used to investigate the outflow and clogging of suspensions of more complex particles.

Impact Statement

Flows of dry and wet granular suspensions through constrictions have long been studied, from the regular discharge of sand in antique hourglasses to the granular flows within silos or even the clogging of particles under confinement. We here describe a novel and versatile two-dimensional microfluidic hopper to investigate the flow and clogging dynamics of dense suspensions. The set-up combines an *in situ* microfluidic fabrication technique with a pneumatic valve at the orifice to print and concentrate particles of controllable shape. We here demonstrate that the microfluidic flow and clogging of dense suspensions of hard monodisperse disk-shaped particles are reminiscent of well-established behaviours in conventional granular hoppers. By conducting experiments under different driving forces, we report a constant particle discharge rate that depends on the flow driving mechanism and follows well-established stochastic clogging laws. Such results might contribute to bridging the gap between dry granular media and dense wet suspensions. Finally, the versatility and tunability of the microfluidic hopper pave the way for systematic experimental studies on complex granular suspensions involving particles of varying shapes and deformability, of obvious interest in practical applications.

---

*These authors contributed equally to this work.

---

1. Introduction

Granular flows through bottlenecks are observed across a wide range of situations, both in nature and industry. These flows can involve dry granular materials, such as in grain silos (Jenike, 1967) and hourglasses (Pongó *et al.* 2021), or particles suspended in a viscous fluid, as found in blood vessels (Patnaik *et al.* 1994) and ink-jet printing processes (Croom *et al.* 2021). Research on particulate flow through a narrow orifice dates back to the mid-1800s, with early studies focusing on the gravity-driven discharge of dry grains from silos (Hagen, 1852; Janssen, 1895). Unlike liquids flowing from a container, grains exit a silo at a constant rate, independent of the filling height. While this constant discharge rate has long been attributed to pressure saturation at the bottom of the silo (Sperl, 2006; Tighe and Sperl, 2007), more recent studies suggest that it is instead due to the constant exit velocity of particles in the outlet region (Aguirre *et al.* 2010).

The dependence of the constant particle discharge rate on the orifice and particle sizes in granular gravity-driven flows is commonly described by the Beverloo law (Beverloo *et al.* 1961). While some of the physical concepts underlying this law have been questioned in recent studies (Janda *et al.* 2012; Mankoc *et al.* 2007; Rubio-Largo *et al.* 2015; Zhou *et al.* 2019), its scaling remains universally observed across a wide range of situations (Nedderman *et al.* 1982). It can even be applied to systems with fundamentally different driving mechanisms, including particles floating at the surface of a flowing fluid (Guariguata *et al.* 2012) or transported on a conveyor belt moving at constant velocity (Aguirre *et al.* 2010). When the orifice size becomes sufficiently small relative to the particle diameter, flow can be impeded by the formation of a clog at the constriction, leading to temporary or permanent interruptions of the discharge process. This phenomenon, observed in both dry systems (Zuriguel, 2014) and suspension flows (Dressaire and Sauret, 2016; Marin and Souzy, 2025), can significantly impact the performance of various industrial processes.

Both the discharge and clogging of particles through a narrow orifice are controlled by a large number of parameters, including the particle size (Beverloo *et al.* 1961; Janda *et al.* 2008), shape (Ashour *et al.* 2017), polydispersity (Zhou *et al.* 2015), deformability (Tao *et al.* 2021) and solid fraction (Vani *et al.* 2022). The roles of channel geometry (Genovese and Sprakel, 2011; Vani *et al.* 2024) and the presence of a liquid phase (Koivisto and Durian, 2017; Marin *et al.* 2018; Souzy and Marin, 2022) have also been analysed. Understanding real flows, which generally involve particles with complex properties, requires the ability to control various of these parameters within the same experimental set-up. Yet, most existing studies rely on pre-existing or commercially available particles, offering limited control over particle properties.

In this paper, we present an experimental model system designed to study the flow of suspensions with tuneable properties through a bottleneck in a two-dimensional configuration. Experiments are performed in a microfluidic hopper channel, where *in situ* fabricated particles are transported through a constriction by a viscous fluid. While our experimental set-up allows for a precise control over particle shape, deformability and volume fraction, this study only focuses on the flow of densely packed, hard, disk-shaped particles. We demonstrate that, despite fundamental differences with dry granular silos, our microfluidic experimental system discharges at a constant rate under both imposed flow rate and pressure conditions. Furthermore, we characterise the discharge rate as a function of particle size under both drivings, and show that the stochastic laws governing particle clogging are recovered. This makes our set-up an effective model system for studying particulate flow through bottlenecks across a wide range of configurations.

The paper is organised as follows: we first present the experimental set-up and particle fabrication method, and characterise the driving force in our system. We then examine the discharge of a dense packing of hard disk-shaped particles, and apply our system to the study of the hopper discharge and the clogging of particles. Finally, we give perspectives for future work involving more complex particle suspensions.

2. Materials and methods

2.1. Experimental set-up

We experimentally study the discharge of a dense suspension of hard disk-shaped particles through a two-dimensional microfluidic hopper. Both particle fabrication and discharge experiments are conducted in a Polydimethylsiloxane (PDMS) channel with fixed length $L = 24$ mm, width $w = 5$ mm and thickness $H = 92$ μm, as depicted in Figure 1(a). The channel features a hopper geometry, with a constriction of varying width $w_c = 600$ or 900 μm, formed by a tapered section with an angle of $45°$. A pneumatically controlled Quake valve (Unger *et al.* 2000) is placed immediately after the constriction, retaining particles while allowing the interstitial fluid to pass when closed. Due to its small thickness relative to its width ($H \ll w$), the microfluidic channel exhibits a Hele-Shaw geometry. The velocity profile is thus parabolic in the z-direction while being independent of the x and y positions, except very close to the sidewalls and in the tapered section.

The microfluidic device consists of three layers (bottom to top): a glass microscopy slide spin coated with PDMS, a thin PDMS slab containing the hopper channel and a thick PDMS slab containing the Quake valve. The two first layers are fabricated by spin coating a $200 - 300$ μm layer of PDMS (Sylgard 184, 19:1 base:cross-linker) onto a glass slide and a hopper channel mould (92 μm SU-8 layer on a silicon wafer), while the third layer is obtained by casting a Quake-valve mould (~ 50 μm SU-8 layer on a silicon wafer) in ~5 mm of PDMS (Sylgard 184, 9:1). All three layers are then cured separately at $70\,°C$ for 40 minutes, after which the Quake valve is bonded to the hopper channel, and the assembly is bonded to the spin-coated glass slide. Bonding is achieved by pressing the layers together and placing the assembly in an oven at $70\,°C$ for 30 minutes (Kool, 2023).

The microfluidic hopper channel is observed using an inverted microscope (Zeiss Axio Observer A1), installed on an optical breadboard (Newport SG breadboard), passively levelled and isolated from vibrations by pneumatic feet (Newport CM-225). The microscope has a UV light (Osram HBO 103W/2), filtered using a band-pass filter at $\lambda = 365 \pm 10$ nm (Chroma D365/10), and reflected into the channel using a reflector cube (Zeiss 424933). The filtered UV light is modulated precisely by an electronic shutter (Uniblitz V25, 100 Hz) coupled to an external signal generator (Agilent A33220A). The channel position is modified using a motorised stage (Märzhäuser Wetzlar Tango PCI-E), which can be operated manually, or digitally via a LabView program. Fluid flow in the microfluidic channel is controlled either by imposing a pressure gradient ΔP with a pressure controller (Fluigent Flow EZ), or by setting a flow rate Q with a syringe pump (Nemesys, Cetoni). For pressure-driven experiments, the tubing length connecting the fluid reservoir to the channel is systematically measured and kept constant to maintain the hydraulic resistance consistent across experiments. Movies of the experiments are recorded at 5 Hz using a digital CMOS camera (Hamamatsu Orca-Fusion C14440).

2.2. Particle fabrication

The particles used in our experiments are fabricated using an *in situ* photo-lithographic projection method (Cappello *et al.* 2019; Dendukuri *et al.* 2007), as described in Figure 1(b). The microfluidic channel is first filled with a UV-polymerisable solution, whose composition depends on the desired deformability of the particles (Duprat *et al.* 2014). In this paper, we limit ourselves to a mixture of 90 % poly(ethylene glycol) diacrylate (PEGDA, $M_N = 575$) and 10 % photo-initiator (Darocur 1173), which results in cross-linked particles with a Young's modulus of ~12 MPa (Cappello *et al.* 2019; Duprat *et al.* 2014), rendering deformations negligible under our experimental conditions. A small amount of surfactant (0.1 % v/v of Tween-80) is added to the polymer solution to mitigate adhesive interactions between particles. The solution is Newtonian of viscosity $\eta = 47$ mPa.s and density $\rho = 1120$ kg.m^{-3}.

Once the channel is filled with the UV-sensitive solution, fluid flow is stopped and the channel is locally exposed to UV light, resulting in the formation of a solid hydrogel-like particle. The cross-linked particle has the same density as the uncross-linked solution and is considered frictionless, since hydrogels have a notoriously low friction coefficient (typically 10^{-3} (Gong, 2006)). Its shape and size
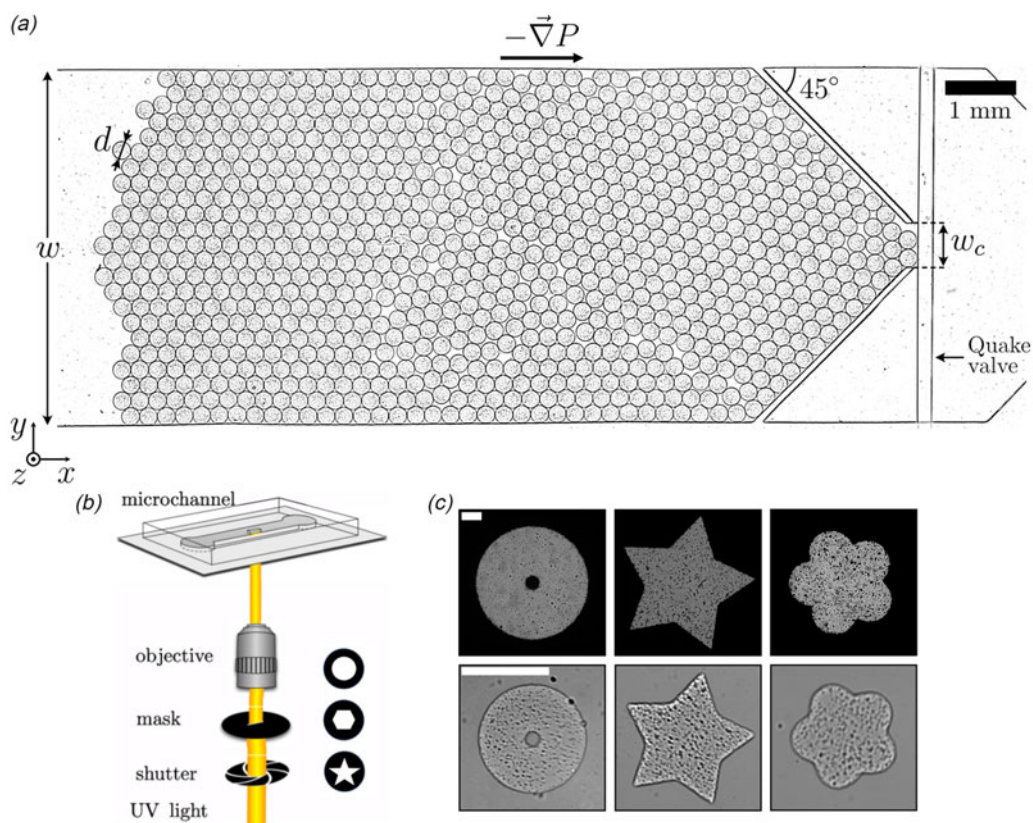
Figure 1. *(a) Top view of the microfluidic hopper channel used in the experiments. The channel consists of a* 24 *mm long straight section of fixed width w = 5 mm, followed by a tapered section with an angle of* 45° *and a constriction width* w_c. *Particles of diameter d are initially packed at the channel constriction using a Quake valve, before being discharged through the constriction. (b) Principle of particle fabrication. A UV curable polymer solution is filled into the microfluidic channel and illuminated through a mask, resulting in hydrogel-like particles being fabricated inside the channel. Image adapted from Cappello et al. (2019). (c) Examples of masks and the corresponding cross-linked particles. Both scale bars are* 200 μm.

are controlled by placing a plastic mask in the field-stop position of the microscope. Due to micrometric speckles on the mask, the particle exhibits textured top and bottom surfaces. This, however, does not influence the experiments, as these surfaces are never in contact with any other particle surface. Examples of masks of various shapes and the corresponding cross-linked particles are given in Figure 1(c). In this study, we only focus on disk-shaped particles with diameters d ranging from 114 to 378 μm. Due to the presence of oxygen near the channel walls, the cross-linking reaction is inhibited over a layer of thickness δ near the top and bottom walls of the channel (Dendukuri *et al.* 2008). This leads to particles with a thickness $h = H - 2\delta$, where δ was estimated to be 21 μm in our experiments, yielding $h = 50$ μm. This thickness is sufficiently large to prevent overlapping and maintain a single layer of particles within the channel.

The microfluidic channel is filled with particles by repeating the aforementioned UV cross-linking and moving the focal spot of the objective between successive UV pulses, enabling precise control over the microscopic particle configuration and initial packing fraction (see Supplementary Movie 1). Since this study focuses on dense packings, particles are fabricated in a hexagonal configuration to maximise their number within the channel. Note that particles must be separated by a few microns during cross-linking to avoid the fusion of closed structures, limiting the maximum packing that can be obtained.

Once the fabrication is complete, particles are densely packed at the constriction of the hopper. This is achieved by closing the Quake valve while imposing a fluid flow, which results in particle accumulation at the orifice (see Supplementary Movie 2).

2.3. Hopper discharge experiment

After the particles are densely packed at the constriction, the Quake valve is opened while maintaining fluid flow, allowing the suspension to discharge through the channel orifice (see Supplementary Movie 3). If a clog forms, a brief reverse flow is applied to break the obstructing arch and restore particle flow (see Supplementary Movie 4). Each experiment concludes when the number of remaining particles is insufficient to fill the tapered section of the channel.

Once recorded, experiment movies are analysed to detect particles and reconstruct their trajectories. For each frame, particles are detected using a fully parallelised in-house convolutional algorithm, with a precision of ~ 0.3 μm. The particle positions are then linked over time using the open-source tracking algorithm trackpy (Allan *et al.* 2024). Particle velocities are calculated using the interframe displacements and the timestamp in the metadata of the images. The number $N(t)$ of particles discharged over time is determined by counting the particles exiting the channel.

In addition to particle trajectories, some experiments require monitoring of the total flow rate Q within the channel during particle discharge. This measurement is particularly useful for estimating the system's hydraulic resistance $R = \Delta P / Q$ in pressure-driven experiments. The use of a flow sensor is not possible here, as such a device would significantly increase the system's resistance to flow. Instead, two alternative measurement methods are employed in this study.

The first and most accurate method consists of measuring the fluid velocity in the channel using micro-particle image velocimetry (PIV). After particle fabrication, the microfluidic channel is filled with tracer particles and transferred to a micro-PIV set-up equipped with a pulsed Nd:YAG laser (Litron Lasers, Nano Series, 532 nm). Fluid velocity is measured in a region far upstream of the orifice, where no particles are present. Due to the small depth of correlation in our micro-PIV set-up, velocity measurements are confined to a z-plane of thickness 18.4 μm, smaller than the channel thickness (Olsen and Adrian, 2000). To calibrate the vertical position of the measurement plane within the channel, we first measure the fluid velocity at different z-positions during a steady flow and fit a parabolic velocity profile (Pimenta *et al.* 2020). The flow rate during particle discharged is then calculated by integrating the measured fluid velocity over the channel cross-section, assuming a parabolic profile in the vertical direction and a uniform velocity along the channel width.

While the micro-PIV method enables precise measurements of Q over time, its use requires switching set-ups and calibration of the vertical position of the measurement plane before each experiment. Additionally, this method does not allow for simultaneous observation of the tapered section during particle discharge. For these reasons, we also use another method, where Q is estimated by measuring the mass m exiting the channel over time. In this method, both the fluid and particles leaving the channel are directed to a precision balance (Denver Instrument TP-214, 0.1 mg accuracy, 1 Hz) via a tubing of diameter 3 mm, sufficiently large to prevent clog formation. The end of the tubing is immersed in a pool of solution to avoid dripping. The total flow rate Q is directly deduced from mass measurements using $Q = \frac{1}{\rho} \frac{\mathrm{d}m}{\mathrm{d}t}$.

2.4. Driving force

A particle in the channel is subject to a pressure force due to the pressure gradient along the channel, a viscous drag force from the fluid flow around it and a viscous friction force in the gaps above and below the particle (Berthet *et al.* 2013). For a disk-shaped particle of radius r and height h in a Hele-Shaw
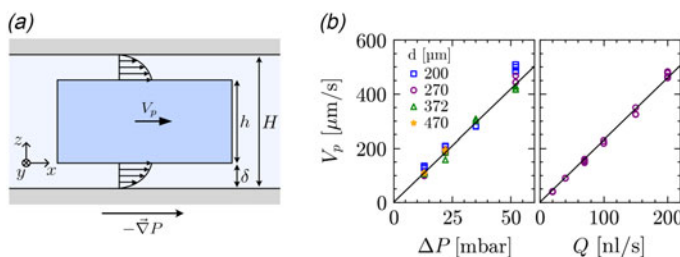
Figure 2. *(a) Schematic side view of a particle with thickness h inside a channel of height H, subjected to a pressure gradient $\vec{\nabla}P$. The particle moves with velocity V_p along the x direction, while the fluid flows through the gaps of thickness $\delta = (H - h)/2$, following a Poiseuille–Couette profile. (b) Measurements of V_p in an empty channel for various particle diameters at different imposed pressure drops ΔP (left panel) and flow rates Q (right panel). The black lines correspond to Equation 4 without any adjusting parameter. In the pressure-imposed case, Q is substituted by $\Delta P/R_0$, where R_0 is the empty channel resistance, measured prior to experimentation using micro-PIV.*

flow, as depicted in Figure 2(a), the pressure force and viscous friction are given by

$$\vec{F}_p = 2h \int_0^\pi P(\theta) r\cos\theta\, \mathrm{d}\theta \vec{e}_x = -\pi h r^2 \frac{\partial P}{\partial x} \vec{e}_x, \tag{1}$$

$$\vec{F}_v = -2\pi r^2 \left(\frac{\delta}{2} \frac{\partial P}{\partial x} + \eta \frac{V_p}{\delta} \right) \vec{e}_x, \tag{2}$$

where δ is the gap thickness, $\partial P/\partial x$ is the pressure gradient along x and V_p is the particle velocity. The viscous drag of the fluid flowing around the disk can be neglected as the fluid and particle velocities are very close to each other in our experimental geometry, where $2\delta \sim h$. The particle velocity can thus be determined by balancing the pressure force with the viscous dissipation in the gaps, yielding

$$V_p = -\frac{\delta(h + \delta)}{2\eta} \frac{\partial P}{\partial x}. \tag{3}$$

This equation shows that particle motion in our system is driven by the pressure gradient along the flow direction, mediated by a geometrical factor and the inverse of the viscosity.

The pressure gradient along x can be expressed as a function of the flow rate Q using the local hydraulic resistance R. In the simple case of a single particle in the straight section of the channel, the particle's influence on the hydraulic resistance can be neglected, and R can be approximated by the resistance of a slit channel with length L, height H and width w, expressed as $R = 12\eta L/(H^3 w)$. Substituting $\partial P/\partial x$ with QR/L, Equation 3 gives

$$V_p = \frac{6\delta(h + \delta)}{H^3} \frac{Q}{w}. \tag{4}$$

Equation 4 demonstrates that the velocity of a single particle in the channel is proportional to the flow rate Q and scales inversely with the channel width w, with a prefactor that depends only on the channel and particle thickness. The validity of this proportionality is verified for varying particle diameters at different imposed flow rates and pressure drops, as shown in Figure 2(b). The black lines represent the predictions of Equation 4 for $H = 92$ μm, $\delta = 21$ μm, $h = 50$ μm and $w = 5$ mm. In the pressure-imposed case, Q is replaced by $\Delta P/R_0$, where $R_0 = 2.7 \times 10^{13}$ Pa.s.m^{-3} is the hydraulic resistance of the microfluidic system in the absence of particles, measured prior to experimentation using micro-PIV.

The driving mechanism in our system differs significantly from commonly studied granular hoppers, such as gravity- or conveyor-belt-driven hoppers. While particles in these systems are driven by a uniform force, the driving force in our microfluidic hopper is dependent on the fluid velocity, which scales inversely with channel width, causing particles to accelerate as they pass through the constriction. Another difference with other systems lies in the temporal variations of the driving force during
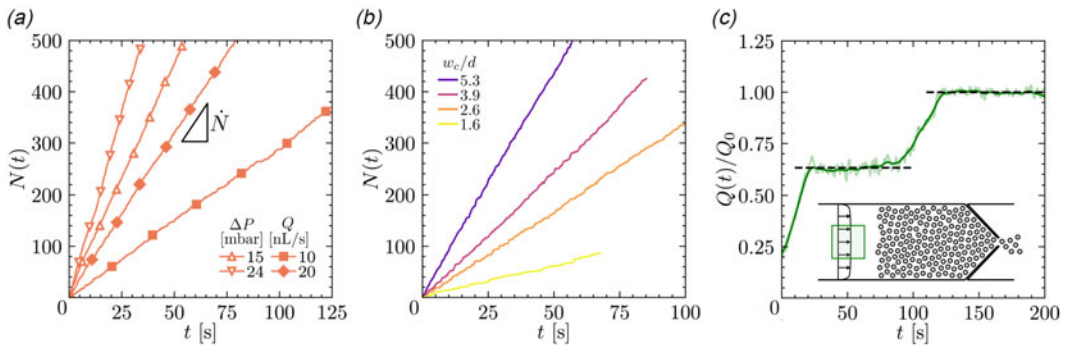
Figure 3. *Discharge curves $N(t)$ for (a) different imposed flow rates Q and pressure drops ΔP at fixed size ratio $w_c/d = 3$, and (b) different orifice-to-particle size ratios w_c/d under a fixed pressure drop $\Delta P = 8$ mbar. All curves present a linear increase in the number of discharged particles N over time. Note that the symbols are used to distinguish the datasets; data were collected at a frequency of 5 Hz. Panel (c) presents micro-PIV measurements of the flow rate $Q(t)$ during a pressure-driven discharge with $\Delta P = 15$ mbar. The flow rate $Q(t)$, deduced from fluid velocity measured in the region highlighted in green, is normalised by Q_0, its final value in an empty channel.*

particle discharge. In most granular hoppers, the driving force remains constant as the channel empties. However, in our microfluidic system, the driving force depends on the overall hydraulic resistance of the channel, which might be influenced by the presence of particles. This complex interplay between fluid flow and particles could potentially lead to a reduction in hydraulic resistance as the hopper empties, resulting in a progressive increase of the driving force during the discharge process. Since the evolution of the outflow rate during the particle discharge is non-trivial, we first studied the discharge of particles from our microfluidic hopper over time.

3. Particle discharge

3.1. Constant discharge rate and hydraulic resistance

We performed discharge experiments with varying particle diameters ($170\,\mu m \leq d \leq 400\,\mu m$), and two orifice widths ($w_c = 600$ and $900\,\mu m$). In each experiment, we either imposed a flow rate, Q, or a pressure drop ΔP, and measured the number $N(t)$ of particles discharged from the channel over time. Figure 3(a) presents typical discharge curves for different imposed flow rates and pressure drops at fixed size ratio $w_c/d = 3$.

For both driving methods, we observe that N scales linearly with time, indicating a constant discharge rate $\dot{N}$. This behaviour is expected under imposed flow rate, as the force exerted by the fluid on particles remains constant throughout the experiment. However, the constant discharge rate under imposed pressure is more surprising, as one would expect the hydraulic resistance R to decrease as the channel empties, leading to a progressive increase of the flow rate. This, in turn, should result in an increasing particle discharge rate, as also reported for gravity-driven submerged granular flows (Koivisto and Durian, 2017; Wilson *et al.* 2014).

The constant discharge rate under imposed pressure conditions suggests that the hydraulic resistance R of our experimental system remains unchanged throughout each experiment, despite the reduction in the number of particles within the channel. To verify this, we measured $Q(t)$ during a pressure-driven discharge experiment ($\Delta P = 15$ mbar) using micro-PIV. In this configuration, particles are not observable, and their number within the channel remains unknown.

Figure 3(c) displays the temporal evolution of $Q(t)/Q_0$ throughout an experiment, with Q_0 representing the final flow rate measured after full discharge. The valve is opened at $t = 0$, and after a brief period (~ 20 s) needed to initiate particle motion, the flow rate stabilises at approximately 60% of Q_0 for
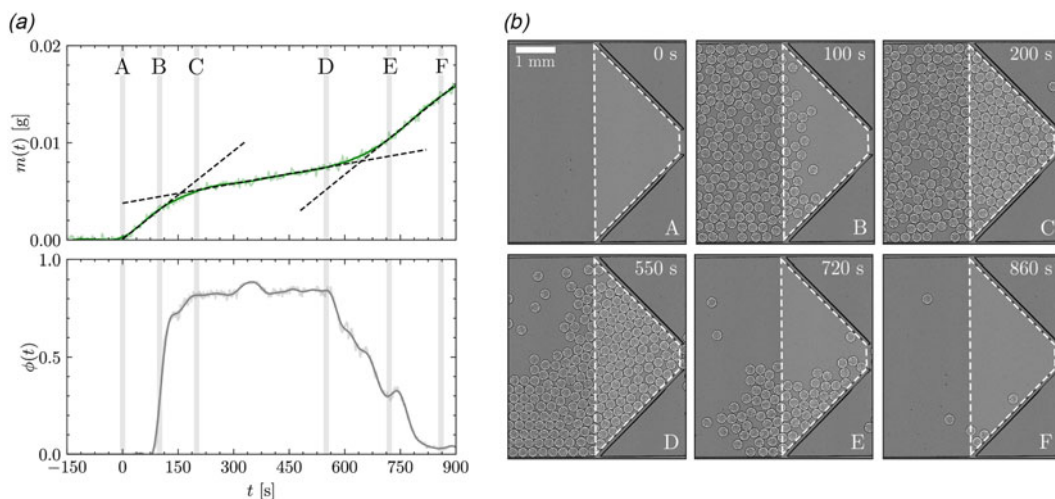
Figure 4. *(a) Temporal evolution of the discharged mass $m(t)$ and the constriction solid fraction $\phi(t)$ during the flow of a dense packing through an empty constriction. The grey vertical lines correspond to the snapshots of the channel shown in (b), labelled from A to F. Measurements of $\phi(t)$ are taken in the area outlined in white in the snapshots.*

approximately a minute, consistent with the typical duration of a discharge under these conditions (see Figure 3(a)). Eventually, the channel completely empties and the flow rate reaches Q_0. Since $R = \Delta P/Q$, this result confirms that the hydraulic resistance remains constant during most of the discharge process. The $\sim 40\,\%$ decrease in Q during particle discharge further indicates that R is not solely controlled by a predominantly high channel resistance, but is also governed by the presence of particles within the channel.

3.2. Hydraulic resistance controlled by particles at the orifice

While the previous experiments clearly demonstrate a constant outflow rate and hydraulic resistance during discharge, attributing this constant flow to the presence of particles is difficult, as we cannot observe particles at the orifice during micro-PIV measurements. To overcome this limitation, we conducted an additional experiment where we observed the flow of a dense particle packing through an empty constriction under imposed pressure conditions, while monitoring the mass of particles and fluid leaving the channel to measure Q.

In this experiment, around 1000 particles were first packed at the orifice, and then gently transported backward by a slight reverse flow, as to not disturb the packing. Once the packing was sufficiently distanced from the orifice (~ 5 mm), both fluid and particle flows were stopped by imposing zero pressure ($t < 0$). At $t = 0$, a pressure drop of $\Delta P = 8$ mbar was applied, driving the particles back towards the constriction. As the packing approached and passed through the tapered section, both the mass $m(t)$ exiting the channel and the solid fraction $\phi(t)$ in the constriction were measured. Mass and solid fraction measurements are presented in Figure 4(a), while the corresponding snapshots of the channel, labelled from A to F, are shown in Figure 4(b). The region used to measure $\phi(t)$ in the constriction is highlighted in white on each snapshot.

Three distinct phases can be identified, each with a constant flow rate, as indicated by the black dashed lines representing linear fits of $m(t)$ in Figure 4(a). During the first phase, the empty constriction (snapshot A) fills with particles as the dense packing enters the constriction (snapshot B), with a fitted flow rate of $Q_1 \approx 27.0$ nl/s. Once the tapered section becomes completely filled with particles, the solid fraction ϕ reaches a maximum value of $\phi \approx 0.83$ (snapshots C and D). During this second phase, ϕ remains constant, except around $t = 350$ s, when a transient clog forms, slightly compacting the particles further.

The second phase is characterised by a significantly reduced flow rate, with a fitted value of $Q_2 \approx 6.0$ nl/s $\approx 0.2Q_1$. Finally, the number of particles within the channel becomes insufficient to completely fill the constriction (snapshot E), and ϕ decreases until nearly no particles remain in the channel (snapshot F). During this final phase, the flow rate rises back to $Q_3 \approx 27.6$ nl/s $\approx 1.02Q_1$.

These results indicate that the flow rate Q and hydraulic resistance R during particle discharge are primarily controlled by the presence of densely packed particles within the tapered section, regardless of the total number of particles in the channel. This suggests that the global behaviour of the system is governed by local processes, with most of the energy dissipation arising from the dense packing being squeezed through the constriction. Energy dissipation may occur through particle rearrangements, particle–wall interactions, or by viscous dissipation due to large velocity fluctuations. Although the exact origin of this dissipation in the tapered section remains to be understood, the constant hydraulic resistance and the subsequent constant discharge rate allow for a comparison with other commonly studied hopper flows. In the next two sections, we will show that our experimental system recovers similar scaling laws for the outflow and clogging of hard monodisperse disks through a constriction as observed in other dry and suspension systems.

4. Applications

4.1. Beverloo-like discharge

As discussed previously, the flow of particles through a bottleneck under gravity is usually described by the Beverloo law. In the two-dimensional (2-D) case, this law is commonly expressed as

$$q_P = C\phi\sqrt{g}(w_c - kd)^{1.5}, \tag{5}$$

where q_P is the particle volumetric discharge rate, ϕ the particle solid fraction and g the acceleration due to gravity, while k and C are two fitting parameters (Beverloo *et al.* 1961). The Beverloo law is based on the assumption that the discharge of particles through a constriction is limited by (i) an effective outlet size $w_c - kd$, which accounts for a no-flow zone along the orifice margins, and (ii) the exit velocity of particles within the orifice, which scales as $\sqrt{g}(w_c - kd)^{0.5}$ under gravity. Although the Beverloo scaling efficiently describes particle discharge in a wide range of configurations, it remains semi-empirical. Subsequent studies have shown that the kd correction arises from density variations near the outlet, and that the particle discharge rate can be derived by integrating the velocity and density profiles along the orifice (Janda *et al.* 2012; Mankoc *et al.* 2007).

In this section, we examine the particle discharge rate in our system and compare the obtained scalings with those observed in conventional systems. To this end, we performed both flow rate- and pressure-driven discharge experiments, varying the driving intensity, orifice width and particle diameter. In each experiment, we determined the discharge rate $\dot{N}$ by fitting the slope of the particle outflow over time, $N(t)$, and deduced the volumetric particle discharge rate $q_p = \dot{N}\pi h d^2/4$. Additionally, we measured the solid fraction ϕ and particle velocity V_{out} at the channel outlet to identify the potential origins of variations in q_p between experiments. In our system, these quantities are related through

$$q_p = \phi h w_c V_{\text{out}}. \tag{6}$$

Figure 5(a) shows ϕ measurements for each experiment, under both imposed flow rate and pressure conditions. The solid fraction at the outlet appears to be solely controlled by the size ratio d/w_c, independent of the nature and intensity of the driving. The variations in ϕ with d/w_c can be described by the linear relationship

$$\phi = \phi_0(1 - k_1 d/w_c), \tag{7}$$

with fitted values $\phi_0 = 0.83$ and $k_1 = 0.78$, suggesting a simple geometric dilution in the tapered section. This dilution has a different origin than in gravity-driven systems, where density variations primarily result from the particles accelerating during their free fall through the orifice (Janda *et al.* 2012).
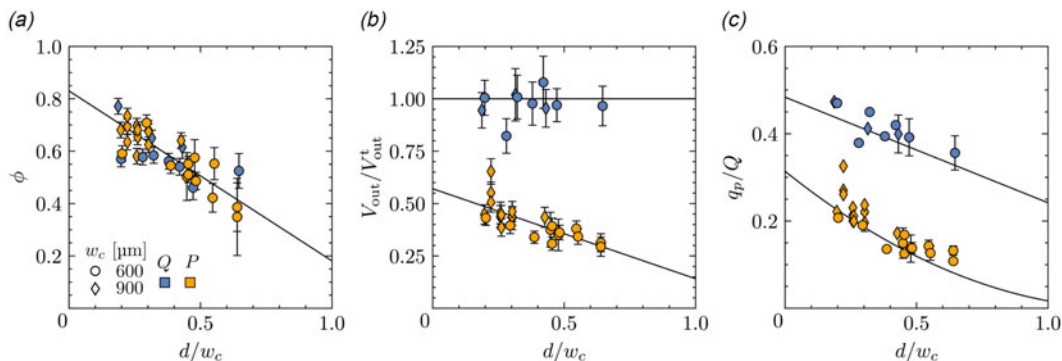
Figure 5. *Experimental measurements under imposed flow rate (blue markers) or pressure drop (orange markers), shown as a function of the size ratio d/w_c. (a) Particle solid fraction at the outlet ϕ, compared with the expression from Equation 7 (solid line). (b) Outlet velocity V_{out}, normalised by the theoretical prediction from Equation 8; solid lines correspond to $V_{\text{out}} = V_{\text{out}}^{\text{t}}$ under imposed flow rate, and to the fit of Equation 9 under imposed pressure. (c) Particle discharge rate, q_p, normalised by the total flow rate Q (flow-rate-driven case) or $Q_0 = \Delta P/R_0$ (pressure-driven case), and compared with Equations 10 and 11.*

The exit particle velocity V_{out} is expected to slightly deviate from the prediction of Equation 4, which was derived for a single particle in an empty channel. The velocity of particles in a freely flowing packing can be obtained by decomposing the system into three layers: a dense particle layer of thickness h at the centre of the channel, where the particles and the interstitial fluid move at a velocity V_p, and two fluid layers of thickness δ above and below the particle layer. The pressure gradient experienced by particles in the packing can be determined by expressing the total flow rate $Q = q_c + q_g$, where q_c and q_g are the flow rates in the central layer and the fluid gaps, respectively. The flow rate in the central layer is given by $q_c = hwV_p$. The flow rate in the gaps is obtained by integrating a Couette–Poiseuille velocity profile with wall velocity V_p in each gap, yielding $q_g = w\delta V_p - (w\delta^3/6\eta)\,\partial P/\partial x$. Substituting V_p from Equation 3, we obtain a relationship between pressure gradient and total flow rate, from which we deduce the theoretical particle velocity at the outlet

$$V_{out}^{\text{t}} = \frac{3(h+\delta)}{\delta^2 + 3(h+\delta)^2}\frac{Q}{w}. \tag{8}$$

Figure 5(b) shows the ratio $V_{\text{out}}/V_{\text{out}}^{\text{t}}$ between measured velocities and theoretical predictions from Equation 8, where Q is replaced by $Q_0 = \Delta P/R_0$ in the pressure-driven case. The results differ significantly depending on the driving mechanism. Under imposed flow rate, V_{out} is independent of the particle diameter and is well described by Equation 8, with an adjusted gap thickness $\delta = 18\ \mu\text{m}$, fitted to account for slight misalignment of particles in the central layer. In contrast, the exit particle velocity under imposed pressure appears to vary with the size ratio d/w_c, with measured values significantly lower than predicted.

Variations in V_{out} are attributed to the coupling between particle outflow and hydraulic resistance under imposed pressure, indicating an increasing energy dissipation with the size ratio d/w_c. Although the precise mechanisms underlying this dissipation remain unclear, its influence on the outlet velocity can be fitted by a linear relationship of the form

$$V_{\text{out}} = \frac{1}{C}V_{\text{out}}^{\text{t}}(1 - k_2 d/w_c), \tag{9}$$

where C reflects the increase in hydraulic resistance due to particle presence in the channel, and k_2 accounts for additional influence of d/w_c. The empirical fit given by Equation 9 is shown in Figure 5(b), with fitted values $C = 1.75$ and $k_2 = 0.75$. We should emphasise that the actual dependence of R and V_{out} on d/w_c is likely more complex than the linear form assumed here.

Incorporating both the variations of ϕ and V_{out} in Equation 6, we obtain two different scalings for the particle discharge rate depending on the driving mechanism. Under imposed flow rate Q, particle dilution at the outlet leads to a Beverloo-like scaling

$$q_P = \phi_0 \frac{3h(h+\delta)}{\delta^2 + 3(h+\delta)^2} \left(1 - k_1 d/w_c\right) Q. \tag{10}$$

This scaling is similar to that obtained in conveyor belt systems, where the outlet velocity is also imposed, and variations of the particle outflow rate stem from changes in the solid fraction near the orifice (Aguirre *et al.* 2010; De-Song *et al.* 2003). Under an imposed pressure drop ΔP, variations of the system resistance add to the outlet dilution, resulting in a nonlinear dependence of the discharge rate on d/w_c

$$q_P = \phi_0 \frac{3h(h+\delta)}{\delta^2 + 3(h+\delta)^2} \left(1 - k_1 d/w_c\right) \left(1 - k_2 d/w_c\right) \frac{\Delta P}{CR_0}. \tag{11}$$

Predicted values of q_P/Q under imposed flow rate and $q_P R_0/\Delta P$ under imposed pressure are compared with experimental measurements for both driving mechanisms in Figure 5(c), showing satisfying agreement.

4.2. Clogging

We now examine the clogging of particles in our experimental set-up. Clogging is usually characterised by the number of particles, s, exiting the channel before clog formation, commonly referred to as the avalanche size. Both experimental (Marin and Souzy, 2025) and theoretical (Helbing *et al.* 2006) studies have widely demonstrated that the avalanche size distribution follows an exponential decay. This behaviour arises from the stochastic nature of clogging, where each particle exiting the channel has an equal probability p_{clog} of forming a clog, resulting in a geometric distribution of the avalanche size probability

$$p(s) = p_{\text{clog}}(1 - p_{\text{clog}})^s. \tag{12}$$

The average avalanche size, $\langle s \rangle$, which is related to the clogging probability by $\langle s \rangle = (1 - p_{\text{clog}})/p_{\text{clog}}$, strongly depends on the ratio of the orifice width w_c to the particle diameter d. In 2-D gravity-driven systems, $\langle s \rangle$ can be described by an exponential-square growth with w_c/d, expressed as

$$\langle s \rangle = A e^{B(w_c/d)^2} - 1, \tag{13}$$

where A and B are two constants (Janda *et al.* 2008; To, 2005).

In this section, we verify that our microfluidic system recovers the same scaling laws for clogging as observed in other systems. To this end, we conducted discharge experiments using disk-shaped particles with diameters ranging from 268 to 378 μm. Particles were discharged through a constriction of width $w_c = 600$ μm, resulting in orifice-to-particle size ratios w_c/d between 1.59 and 2.24. The discharge experiments were pressure driven ($\Delta P = 8$ mbar) rather than flow rate driven, as pressure controllers have a faster response time than syringe pumps. We considered that the channel was clogged when an arch of particles formed at the constriction and persisted for more than 3 s, exceeding the maximum Stokes time near the outlet measured across all experiments ($\tau = d/V_p \approx 2$ s). Since all clogging arches were broken after 3 s, the lifetime of clogs in our set-up was not investigated. However, the fraction of transient clogs in our system is expected to be reduced compared with previously studied systems (Souzy *et al.* 2020; Souzy and Marin, 2022), due to the 2-D geometry and the presence of gaps above and below the particle layer.

For each particle size considered, the avalanche size distribution $N(s)$ was determined by measuring s over a large number of clogs. Avalanches with fewer than four particles were excluded, as they may involve pre-existing clogging arches. Each distribution can be described by an exponential fit, as indicated by the black line in Figure 6(a) for $w_c/d = 1.59$. We verified that all distributions collapsed on the same exponential law when normalised by the average avalanche size (Figure 6(b)), consistent with prior studies. Additionally, we show in Figure 6(c) that the evolution of $\langle s \rangle$ with w_c/d in our experimental
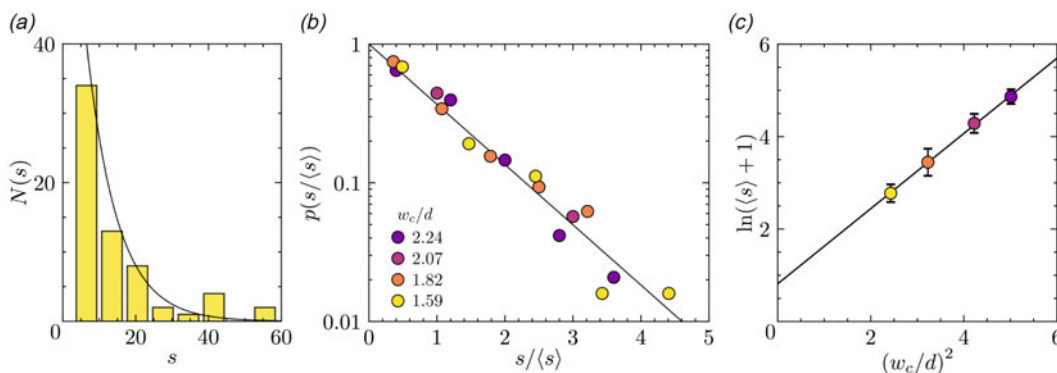
Figure 6. *(a) Histogram showing the number of events N in which s particles escape the channel before clog formation, for a fixed size ratio $w_c/d = 1.59$. The solid line represents an exponential distribution. (b) Probability distribution function of the normalised avalanche size $s/\langle s \rangle$ for all size ratios considered, fitted with an exponential law. (c) Plot of $ln(\langle s \rangle + 1)$ as a function of $(w_c/d)^2$. The solid line is a linear fit, and error bars are obtained using a bootstrapping method applied to each dataset. All experiments were performed under a fixed pressure drop $\Delta P = 8$ mbar.*

set-up is consistent with the scaling of Equation 13, with $\ln(\langle s \rangle + 1)$ increasing linearly with $(w_c/d)^2$ across the range of orifice-to-particle size ratios considered. Note that $\langle s \rangle$ is calculated by dividing the total number of discharged particles by the total number of clogs detected for a given particle size. This method is more accurate than averaging s over all clogging events, as the latter approach excludes large avalanches that do not result in a clog.

4.3. Perspectives

In this paper, we focused exclusively on the flow of hard, monodisperse disk-shaped particles to characterise our experimental system and compare it with other well-established systems. However, the versatility of our experimental set-up makes it an excellent model system for exploring more complex scenarios. In the following paragraphs, we outline perspectives for future works on hopper flow, and more broadly, in any 2-D flow configuration.

The shape of particles can be easily controlled in our experimental set-up by changing the design of the UV mask used during particle fabrication. This method provides a fast and effective way of varying particle shape, opening new perspectives for studying the flow dynamics of non-circular grains. The fine and rapid control over particle shape enables systematic studies of shape properties through gradual changes, such as by precisely adjusting the aspect ratio of elongated particles, as seen in Figure 7(a). Since there is no flow during the fabrication process, particles with different shapes can also be combined by first printing a batch of particles, then changing the UV mask and printing another batch in the remaining spaces. This method can be applied to fabricate circular particles with finely controlled polydispersity, or even mixtures of particles with different shapes, as illustrated in Figure 7(b) for a disk–fibre mixture.

In addition to particle shape, our experimental set-up provides a relatively precise way to modulate particle deformability, either by changing the composition of the cross-linking solution (Duprat *et al.* 2014), or by fabricating thin, slender structures that can deform under flow (Cappello *et al.* 2019). More complex situations combining particles of different deformability can also be achieved, as illustrated in Figure 7(c), where hard disks are embedded within flexible rings (see Supplementary Movie 5). Although all the examples provided involve dense packings, dilute configurations can also be achieved with our experimental system, as the *in situ* fabrication method provides precise control over the spatial distribution of particles before flow.
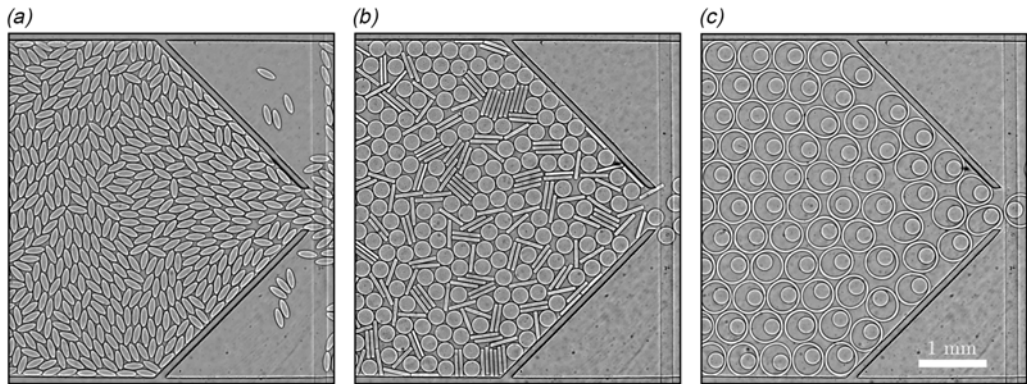
Figure 7. *Examples of discharge experiments with (a) elongated grains, (b) a mixture of disks and rigid fibres and (c) disks embedded within flexible rings (see Supplementary Movie 5).*

5. Conclusion

In this paper, we presented a 2-D microfluidic set-up designed to investigate the flow and clogging of particles in confined geometries. This innovative set-up relies on an *in situ* particle fabrication method, which enables easy and precise control over the particle shape, deformability and volume fraction. Experiments were conducted in a microfluidic hopper channel, where a Quake valve positioned immediately after the constriction was used to concentrate particles up to the maximum packing fraction. Our study focused on the flow of a dense packing of hard, monodisperse, disk-shaped particles through a bottleneck under both imposed flow rate and pressure conditions.

We have shown that, despite fundamental differences between our microfluidic system and typical dry granular systems, particles discharge at a constant rate under both imposed flow rate and pressure conditions in our experimental set-up. This constant particle outflow rate arises from the fact that the hydraulic resistance is constant during the entire discharge, and dominated by the presence of densely packed particles within the tapered section of the hopper. We also demonstrated by measuring the particle discharge rate for varying driving intensities, particle diameters and constriction widths that the outflow of particles in our system depends on the flow driving mechanism. While the discharge follows a Beverloo-like scaling under imposed flow rate due to particle dilution at the orifice, it exhibits a nonlinear dependence on the particle-to-outlet size ratio under imposed pressure, resulting from both outlet dilution and a coupling between particle outflow and channel resistance. Finally, we showed that the statistics of clog formation in our experimental system follow the same stochastic laws as reported in other systems.

The good agreement between our experimental results and other commonly studied systems proves its utility in studying the discharge and clogging of particulate suspensions in various 2-D configurations. The versatility of our microfluidic system allows for future investigation of the role of particle shape, size distribution and deformability in the outflow and clogging of suspended particles through a bottleneck.

Competing interests. The authors declare no competing interests.

References

Aguirre, M. A., Grande, J. G., Calvo, A., Pugnaloni, L. A., & Géminard, J.-C. (2010). Pressure independence of granular flow through an aperture. *Physical Review Letters*, *104*(23), 238002.

Allan, D. B., Caswell, T., Keim, N. C., van der Wel, C. M., & Verweij, R. W. (2024). soft-matter/trackpy:v0.6.4.

Ashour, A., Wegner, S., Trittel, T., Börzsönyi, T., & Stannarius, R. (2017). Outflow and clogging of shape-anisotropic grains in hoppers with small apertures. *Soft Matter*, *13*(2), 402–414.

Berthet, H., Fermigier, M., & Lindner, A. (2013). Single fiber transport in a confined channel: Microfluidic experiments and numerical study. *Physics of Fluids*, *25*(10), 103601. 103601–15

Beverloo, W. A., Leniger, H. A., & van de Velde, J. (1961). The flow of granular solids through orifices. *Chemical Engineering Science*, *15*(3), 260–269.

Cappello, J., Bechert, M., Duprat, C., du Roure, O., Gallaire, F., & Lindner, A. (2019). Transport of flexible fibers in confined microchannels. *Physical Review Fluids*, *4*(3), 034202.

Croom, B. P., Abbott, A., Kemp, J. W., Rueschhoff, L., Smieska, L., Woll, A., Stoupin, S., & Koerner, H. (2021). Mechanics of nozzle clogging during direct ink writing of fiber-reinforced composites. *Additive Manufacturing*, *37*, 101701.

De-Song, B., Xun-Sheng, Z., Guang-Lei, X., Zheng-Quan, P., Xiao-Wei, T., & Kun-Quan, L. (2003). Critical phenomenon of granular flow on a conveyor belt. *Physical Review E*, *67*(6), 062301.

Dendukuri, D., Gu, S. S., Pregibon, D. C., Hatton, T. A., & Doyle, P. S. (2007). Stop-flow lithography in a microfluidic device. *Lab on a Chip*, *7*(7), 818–828.

Dendukuri, D., Panda, P., Haghgooie, R., Kim, J. M., Hatton, T. A., & Doyle, P. S. (2008). Modeling of oxygen-inhibited free radical photopolymerization in a PDMS microfluidic device. *Macromolecules*, *41*(22), 8547–8556.

Dressaire, E., & Sauret, A. (2016). Clogging of microfluidic systems. *Soft Matter*, *13*(1), 37–48.

Duprat, C., Berthet, H., Wexler, J. S., du Roure, O., & Lindner, A. (2014). Microfluidic in situ mechanical testing of photopolymerized gels. *Lab on a Chip*, *15*(1), 244–252.

Genovese, D., & Sprakel, J. (2011). Crystallization and intermittent dynamics in constricted microfluidic flows of dense suspensions. *Soft Matter*, *7*(8), 3889–3896.

Gong, J. P. (2006). Friction and lubrication of hydrogels—its richness and complexity. *Soft Matter*, *2*(7), 544–552.

Guariguata, A., Pascall, M. A., Gilmer, M. W., Sum, A. K., Sloan, E. D., Koh, C. A., & Wu, D. T. (2012). Jamming of particles in a two-dimensional fluid-driven flow. *Physical Review E*, *86*(6), 061311.

Hagen, G. (1852). Druck und bewegung des trockenen sandes. *Berliner Monatsberichte der Akademie der Wissenschaften*, *10*(1), 35–42.

Helbing, D., Johansson, A., Mathiesen, J., Jensen, M. H., & Hansen, A. (2006). Analytical approach to continuous and intermittent bottleneck flows. *Physical Review Letters*, *97*(16), 168001.

Janda, A., Zuriguel, I., Garcimartín, A., Pugnaloni, L. A., & Maza, D. (2008). Jamming and critical outlet size in the discharge of a two-dimensional silo. *Europhysics Letters*, *84*(4), 44002.

Janda, A., Zuriguel, I., & Maza, D. (2012). Flow rate of particles through apertures obtained from self-similar density and velocity profiles. *Physical Review Letters*, *108*(24), 248001.

Janssen, H. (1895). Versuche uber getreidedruck in silozellen. *Zeitschrift des Vereins Deutscher Ingenieure*, *39*, 1045.

Jenike, A. W. (1967). Quantitative design of mass-flow bins. *Powder Technology*, *1*(4), 237–244.

Koivisto, J., & Durian, D. J. (2017). The sands of time run faster near the end. *Nature Communications*, *8*(1), 15551.

Kool, L. (2023). Microfluidic flow of suspensions of deformable particles through constrictions. Physics [physics]. Université Paris Cité. English. ffNNT: 2023UNIP7103ff. fftel-04579326f.

Mankoc, C., Janda, A., Arévalo, R., Pastor, J. M., Zuriguel, I., Garcimartín, A., & Maza, D. (2007). The flow rate of granular materials through an orifice. *Granular Matter*, *9*(6), 407–414.

Marin, A., Lhuissier, H., Rossi, M., & Kähler, C. J. (2018). Clogging in constricted suspension flows. *Physical Review E*, *97*(2), 021102.

Marin, A., & Souzy, M. (2025). Clogging of noncohesive suspension flows. *Annual Review of Fluid Mechanics*, *57*, 89–116.

Nedderman, R. M., Tüzün, U., Savage, S. B., & Houlsby, G. T. (1982). The flow of granular materials—I: Discharge rates from hoppers. *Chemical Engineering Science*, *37*(11), 1597–1609.

Olsen, M. G., & Adrian, R. J. (2000). Out-of-focus effects on particle image visibility and correlation in microscopic particle image velocimetry. *Experiments in Fluids*, *29*(1), S166–S174.

Patnaik, J. K., Das, B. S., Mishra, S. K., Mohanty, S., Satpathy, S. K., & Mohanty, D. (1994). Vascular clogging, mononuclear cell margination, and enhanced vascular permeability in the pathogenesis of human cerebral malaria. *The American Journal of Tropical Medicine and Hygiene*, *51*(5), 642–647.

Pimenta, F., Toda-Peters, K., Shen, A. Q., Alves, M. A., & Haward, S. J. (2020). Viscous flow through microfabricated axisymmetric contraction/expansion geometries. *Experiments in Fluids*, *61*(9), 204.

Pongó, T., Stiga, V., Török, J., Lévay, S., Szabó, B., Stannarius, R., Hidalgo, R. C., & Börzsönyi, T. (2021). Flow in an hourglass: Particle friction and stiffness matter. *New Journal of Physics*, *23*(2), 023001.

Rubio-Largo, S. M., Janda, A., Maza, D., Zuriguel, I., & Hidalgo, R. C. (2015). Disentangling the free-fall arch paradox in silo discharge. *Physical Review Letters*, *114*(23), 238002.

Souzy, M., & Marin, A. (2022). Role of liquid driving on the clogging of constricted particle suspensions. *Journal of Fluid Mechanics*, *953*, A40.

Souzy, M., Zuriguel, I., & Marin, A. (2020). Transition from clogging to continuous flow in constricted particle suspensions. *Physical Review E*, *101*(6), 060901.

Sperl, M. (2006). Experiments on corn pressure in silo cells—translation and comment of Janssen's paper from 1895. *Granular Matter*, *8*(2), 59–65.

Tao, R., Wilson, M., & Weeks, E. R. (2021). Soft particle clogging in two-dimensional hoppers. *Physical Review E*, *104*(4), 044909.

Tighe, B. P., & Sperl, M. (2007). Pressure and motion of dry sand: Translation of Hagen's paper from 1852. *Granular Matter*, *9*(3), 141–144.

To, K. (2005). Jamming transition in two-dimensional hoppers and silos. *Physical Review E*, *71*(6), 060301.

Unger, M. A., Chou, H. P., Thorsen, T., Scherer, A., & Quake, S. R. (2000). Monolithic microfabricated valves and pumps by multilayer soft lithography. *Science (New York, N.Y.)*, *288*(5463), 113–116.

Vani, N., Escudier, S., Jeong, D.-H., & Sauret, A. (2024). Role of the constriction angle on the clogging by bridging of suspensions of particles. *Physical Review Research*, *6*(3), L032060.

Vani, N., Escudier, S., & Sauret, A. (2022). Influence of the solid fraction on the clogging by bridging of suspensions in constricted channels. *Soft Matter*, *18*(36), 6987–6997.

Wilson, T. J., Pfeifer, C. R., Meysingier, N., & Durian, D. J. (2014). Granular discharge rate for submerged hoppers. *Papers in Physics*, *6*(2), 060009.

Zhou, Y., Lagrée, P.-Y., Popinet, S., Ruyer, P., & Aussillous, P. (2019). Gas-assisted discharge flow of granular media from silos. *Physical Review Fluids*, *4*(12), 124305.

Zhou, Y., Ruyer, P., & Aussillous, P. (2015). Discharge flow of a bidisperse granular media from a silo: Discrete particle simulations. *Physical Review E*, *92*(6), 062204,

Zuriguel, I. (2014). Invited review: Clogging of granular materials in bottlenecks. *Papers in Physics*, *6*, 060014.